

## Nonreciprocal Elastic Wave Beaming in Dynamic Phased Arrays

M. Moghaddaszadeh<sup>1,2</sup>, R. Adlakha<sup>1</sup>, M.A. Attarzadeh<sup>1</sup>, A. Aref<sup>1</sup>, and M. Nouh<sup>1,2,\*</sup>

<sup>1</sup>*Department of Civil, Structural and Environmental Engineering, University at Buffalo (SUNY), Buffalo, New York 14260-4300, USA*

<sup>2</sup>*Department of Mechanical and Aerospace Engineering, University at Buffalo (SUNY), Buffalo, New York 14260-4400, USA*



(Received 23 June 2021; revised 5 August 2021; accepted 24 August 2021; published 20 September 2021)

Beam forming using phased arrays forms the basis of several sonar communication and biomedical imaging techniques. However, to date, such arrays remain constrained by wave reciprocity in addition to being confined to their operational frequency; two limitations that have severely hindered imaginative advancements in this domain. In the context of sound propagation, nonreciprocity typically refers to unidirectional elastic and surface acoustic wave devices. However, a breakage of reciprocity in phased arrays manifests itself in reception and transmission patterns, which can be independently tuned, which has thus far been elusive. This work reports on a class of nonreciprocal phased arrays, which operate independently and simultaneously within different directions and frequency channels, thus breaking transmission-reception symmetry and offering enhanced capabilities in guided wave engineering. The system comprises an array of transceiving piezoelectric wafer discs bonded to an elastic medium and incorporates a prescribed dynamic modulation on top of a static phase gradient, which enables concurrent phononic transitions in energy and momentum spaces that mitigate the constraints imposed by Lorentz reciprocity. Following the theory and predictive analysis, the entire array and its associated capabilities are demonstrated experimentally.

DOI: 10.1103/PhysRevApplied.16.034033

### I. INTRODUCTION

Guided elastic waves have been a cornerstone of structural health monitoring and nondestructive testing for decades owing to their superior sensitivity to defects [1–3]. They have also been adopted in medical applications due to their low damping, allowing them to travel long distances without dissipation [4], and to manipulate the direction of incident waves via diffraction gratings [5,6] and metasurfaces [7]. As one of the most prevalent methods for guided wave engineering, surface-mounted piezoelectric arrays allow efficient wave beaming [8] and sensing [9] in one self-contained configuration. Phased arrays are a union of multiple wave transmitting and receiving elements (*transceivers*) arranged in one- (linear), two- (planar), or three- (hemispherical) dimensional configurations [10,11]. Conventional phased arrays can transmit elastic waves in a desired direction via constructive and destructive interferences between the emitted wave fields from different array elements. The augmented phase of the individual elements can be controlled to instigate wave beaming in transmission and reception in 2D and 3D spaces without requiring moving mechanical parts [12]. For example,

by incorporating a quasistatically changing phase gradient, existing phased arrays are capable of electronically steering a wave beam across the whole field of view [13]. Alternatively, by carefully designing the spatial distribution of their phase gradients, phased arrays can be used to focus wave energy at a specific point and create standing waves to trap particles or levitate objects [14]. In offering a wide portfolio of wave-forming capabilities, phased arrays provide a versatile platform, which can be exploited in a wide range of acoustic engineering applications [15–17]. Notable among these are fault detection in elastic media [18–21], identification of pipe damage [22,23], wind sensing [24], and more recently, in creating high-resolution 3D images of internal structural defects [25]. Nonlinear subharmonics and higher-harmonic ultrasonic phased arrays are now being proposed for imaging of internal closed cracks [26–28]. In the latter, however, all nonlinear harmonics ought to be received by a single phased array to obtain all the images needed and detect the open and closed portions of a crack. A traditional ultrasonic phased array, which can only operate in a single channel, is simply incapable of fulfilling this objective [29]. Recently, fundamental wave amplitude difference (FAD) was suggested that uses both fixed- [30–32] and different-voltage [33,34] approaches to address this issue by measuring the incident amplitude dependence of the fundamental wave

\*mnouh@buffalo.edu

component. Nevertheless, a more robust and straightforward strategy remains of great interest and can potentially reshape the future course of experimental structural health evaluation.

Reciprocity is one of the fundamental principles of wave propagation that often constrains the operation of phased arrays. It implies that transmission between two spatially separated locations in linear time-invariant (LTI) systems remains the same with an interchange of the actuating and sensing points [35]. An intentional breakage of this constraint opens up untapped opportunities and has understandably found applications in various fields of engineering ranging from electromagnetics [36–39], to acoustics [40–45] and elasticity [46–49]. The injection of prescribed temporal variations in systems with a spatial-gradient (with the intention of breaking time-reversal symmetry) has been demonstrated as a favorable approach due to its independence on signal intensity and its ability to be replicated in a finite practical setting [50–52]. There are a number of studies pertaining to photonic metasurfaces, where a nonreciprocal behavior is observed by incorporating a space-time-periodic (STP) modulation of properties [53–56]. However, there are very few efforts of electromagnetic phased arrays, which integrate such modulations with the underlying gradient [57]. The concept of nonreciprocity is often narrowly used to describe unidirectional wave propagation and diodelike systems. Owing to reciprocal symmetry, existing phased arrays are sensitive only to incident waves arriving from the same exact direction as those it can transmit to; a phenomenon that effectively guarantees identical radiation and reception patterns [58]. As a result, the notion of nonreciprocity in phased-array platforms potentially manifests itself in the form of non-identical radiation and reception beam-forming patterns, which can be independently tuned [59,60].

This work presents a class of phased arrays, which operate independently and simultaneously within different directions and frequency channels, thus breaking transmission-reception symmetry and offering superior capabilities in guided wave engineering. In the elastic domain, the experimental realization of such a system has thus far been elusive [61]. Without loss of generality, the array is comprised of an array of transceiving piezoelectric wafer discs (PWDs), which undergo dynamic phase modulation on top of a static phase gradient. Contrary to conventional arrays, the proposed system incorporates a dynamic modulation on top of the underlying static phase gradient resulting in a modified time-delay law, which brings about two unprecedented functions: (1) A capability to generate several beams which can be steered independently (i.e., multiple momentum channels). (2) In the absence of advanced (and often time-consuming) accommodations to operate within wide-band and nonlinear regimes, the system presented here invokes multiple frequency channels that can be each individually tuned

such that all required data can be derived with a single measurement without the need for any sub- or superharmonic postprocessing schemes. The combined multiple momentum and frequency channels within the array not only prompt faster scanning (as the time required to scan the complete domain is inversely proportional to the number of simultaneous momentum channels), but also enables concurrent measurements of distinct frequency content for different channels in both transmission and reception operations. Finally, we report on the array's capability of inducing increasingly nonreciprocal radiation and reception patterns *in situ*. The entire array and its associated capabilities are demonstrated experimentally, confirming the theoretical framework established here and setting a road map for broader future implementation.

## II. THEORY OF DYNAMIC ELASTOACOUSTIC PHASED ARRAY

The proposed STP PWD phased array breaks time-reversal symmetry via a space-time variation of phase gradient, which selectively alters directional and frequency content of various harmonics generated by the array, as illustrated in Fig. 1. A transceiver of the proposed phased array comprises a single PWD coupled with a phase shifter. Consider a dynamic phase angle for the  $n$ th PWD of the following STP form:

$$\phi_n(t) = \kappa_c y_n + \delta \cos(\omega_m t - \kappa_m y_n), \quad (1)$$

where  $y_n$  is the  $y$  coordinate of the  $n$ th PWD along the array as depicted in Fig. 1(a).  $\kappa_c$  is the static phase gradient (also present in conventional phased arrays),  $\delta$  denotes the STP modulation depth,  $\omega_m$  and  $\kappa_m$  are the temporal and spatial modulation frequencies, respectively. The figure also shows the array with  $N$  PWDs surface mounted on a thin plate and linearly distributed with a pitch  $d$ .

### A. Transmission

When transmitting, the array is excited with an input voltage of the form  $V_0 e^{-i\omega t}$ , where  $V_0$  is the amplitude,  $i = \sqrt{-1}$ , and  $\omega$  is the temporal frequency. Subsequently, each phase shifter augments this signal with the STP phase angle described by Eq. (1),  $v_n(t) = V_0 e^{i[-\omega t + \phi_n(t)]}$ . The supplied voltage to the  $n$ th PWD, thus becomes

$$v_n(t) = V_0 e^{i(-\omega t + \kappa_c y_n)} e^{i\delta \cos(\omega_m t - \kappa_m y_n)}. \quad (2)$$

Using the Jacobi-Anger expansion, this can be replaced with an infinite series of Bessel functions. Upon further simplification, we get

$$v_n(t) = V_0 \sum_{q=-\infty}^{\infty} i^q J_q(\delta) e^{i(-\omega^{(q)} t + \kappa_c^{[q]} y_n)}, \quad (3)$$

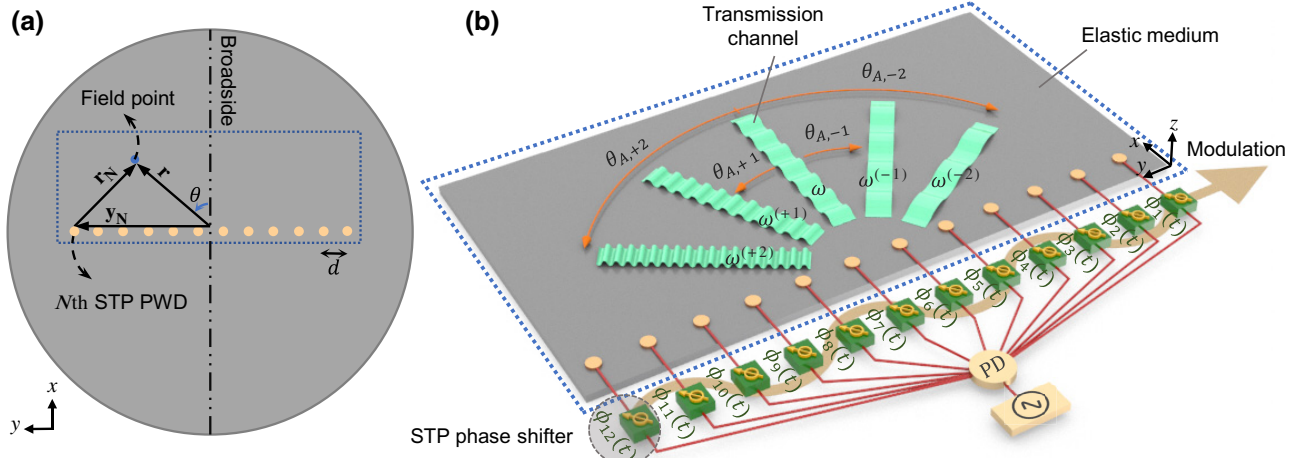


FIG. 1. STP PWD phased-array surface mounted on a thin aluminum plate. (a) Coordinate system and array geometry. (b) Schematic diagram of the different array components including piezoelectric discs, STP phase shifters, power divider (PD), and voltage generator. Different harmonics are generated and propagate in different directions.

where  $\mathbb{J}_q(\bullet)$  is a  $q$ th-order Bessel function of the first kind and  $(\bullet)^{(q)}$  and  $(\bullet)^{[q]}$  are shorthand notations for a frequency shift of  $+q\omega_m$  and a phase gradient shift of  $+q\kappa_m$ , respectively, i.e.,  $\omega^{(q)} = \omega + q\omega_m$  and  $\kappa_c^{[q]} = \kappa_c + q\kappa_m$ . Applying this voltage to the  $n$ th PWD generates a radial strain, which is transferred to the substrate plate through the shear coupling of the bonding layer. This shear-stress excitation induces Lamb waves with a displacement distribution on the top surface of the plate,  $w_n(r_n, t)$ . The total far-field out-of-plane displacement field is then computed by adding the field generated by the individual STP PWDs, i.e.,  $w_{\text{net}}(r, t) = \sum_{n=1}^N w_n(r_n, t)$ . Here,  $r$  is the radial distance from the center of the array to a field point and  $r_n$  is the radial distance between the center of the  $n$ th PWD to the same field point as per Fig. 1(a). The total far-field out-of-plane displacement field, thus becomes (see Note S1 within the Supplemental Material for a detailed derivation [62])

$$w_{\text{net}}(r, \theta, t) \cong Ne^{-i(\pi/4)} \sqrt{\frac{2}{\pi r}} \sum_{q=-\infty}^{\infty} \left[ \frac{B_S^{(q)}}{\sqrt{k_S^{(q)}}} D_{S,q}(\theta) \psi_S^{(q)}(r, t) + \frac{B_A^{(q)}}{\sqrt{k_A^{(q)}}} D_{A,q}(\theta) \psi_A^{(q)}(r, t) \right], \quad (4)$$

where  $(r, \theta)$  are the polar coordinates of a field point of interest with respect to the center of the array, while  $\theta$  is measured counterclockwise from broadside, as shown in Fig. 1(a).  $k_\alpha^{(q)}$  is the frequency-shifted wave number of the first symmetric (or antisymmetric) Lamb wave, for  $\alpha = S$  (or  $\alpha = A$ ), and  $B_\alpha^{(q)}$  is the associated amplitude coefficient (see Note S1 within the Supplemental Material for more details [62]). In Eq. (4),  $\psi_\alpha^{(q)}(r, t) = e^{i(-\omega^{(q)}t + k_\alpha^{(q)}r)}$

denotes a symmetric (for  $\alpha = S$ ) or antisymmetric (for  $\alpha = A$ ) spherical Lamb wave with a unit amplitude. Due to the elliptical motion of material particles in both symmetric and antisymmetric Lamb waves, the two are naturally coupled and Eq. (4) confirms that they appear alongside one another in out-of-plane deformations. Further,  $D_{\alpha,q}(\theta)$  represents  $q$ th-order modified transmission directivities of the array for the first symmetric and antisymmetric Lamb waves as follows:

$$D_{\alpha,q}(\theta) = i^q \mathbb{J}_q(\delta) \frac{\sin \left[ (Nd/2)(k_\alpha^{(q)} \sin \theta - \kappa_c^{[q]}) \right]}{N \sin \left[ (d/2)(k_\alpha^{(q)} \sin \theta - \kappa_c^{[q]}) \right]}, \quad \alpha = S, A. \quad (5)$$

An inspection of Eq. (4) and  $\psi_\alpha^{(q)}(r, t)$  reveals that in addition to the fundamental mode, an infinite set of harmonics of both first Lamb waves travel in the structure with different frequencies and wave numbers, effectively acting as different transmission channels. The amplitude, wave number, and directional behavior of these channels primarily depends on the phase angle parameters and are *in situ* tunable to achieve a desired performance (see Note S2 within the Supplemental Material [62]). A  $q$ th-order transmission channel, however, is not equally strong in every direction  $\theta$ . Its propagation strength along any direction  $\theta$  can be quantified using its  $D_{\alpha,q}(\theta)$  function (see Note S3). Practically, we are able to define principal transmission directions for both symmetric and antisymmetric Lamb waves as the  $\theta$ -values which maximize the respective directivities and corresponding wave amplitudes. Using Eq. (5), we determine the  $q$ th-order ( $q \in \mathbb{Z}$ ) principal transmission directions for the first Lamb waves to be  $\theta_{\alpha,q} = \sin^{-1}(\kappa_c^{[q]}/k_\alpha^{(q)})$  with  $\alpha = S, A$ . In the most general

case,  $k_S^{(q)}$  and  $k_A^{(q)}$  can only be computed after numerically solving the symmetric and antisymmetric Rayleigh-Lamb equations for a given  $\omega^{(q)}$  [63]; however, for sufficiently small values of  $h\omega^{(q)}/2\pi \leq 100$  kHz mm, where  $h$  is the plate thickness, the first symmetric and antisymmetric Lamb waves asymptotically approach the behavior of extensional and flexural plate waves and  $k_{S,A}$  can then be approximated accordingly [1]. As such, to facilitate an analytical solution, we limit our analysis to systems where the frequency-shifted symmetric wave number is  $k_S^{(q)} = \omega^{(q)}\sqrt{\rho(1-\nu^2)/E}$  and the frequency-shifted antisymmetric wave number is  $k_A^{(q)} = \sqrt{\omega^{(q)}}[12\rho(1-\nu^2)/Eh^2]^{1/4}$ . Here,  $E$  is the modulus of elasticity,  $\nu$  is Poisson's ratio and  $\rho$  is the plate material density. We note that the flexural waves predominantly result in out-of-plane shear deformations, while extensional waves breed in-plane displacements. As such, we focus here on out-of-plane deformations resulting from antisymmetric flexural waves in plates. The top panel of Fig. 2 illustrates the transmission behavior of the STP PWD phased array operating at two modulation depths,  $\delta = 1.5$  and  $\delta = 2.4$  predicted by both theory and simulations. Here, a 6-m radius thin circular plate ( $h = 1.27$  mm thickness) is used as an elastic medium. Finite-element (FE) simulations are conducted up to 0.02 s, which is less than the time waves needed to reach the boundaries to avoid reflections, thus enabling a 0.05 kHz resolution in the frequency spectrum. The plate is made of aluminum with the following parameters:  $E = 73.1$  GPa,  $\nu = 0.33$ , and  $\rho = 2780$  kg/m<sup>3</sup>. The first antisymmetric Lamb wave is generated using 12 STP PWDs each having an  $a = 4$  mm radius. A quarter-wavelength pitch is used, i.e.,  $d = 16$  mm. The PWDs are excited with a fundamental frequency of  $\omega/2\pi = 3$  kHz. The effect of STP phase shifters is implicitly included in the voltage provided to the PWDs using the following set of parameters:  $\omega_m/2\pi = 0.05$  kHz,  $\kappa_c = 0$  and  $\kappa_m = 20.4808\pi$  rad/m. As a result, each group of six STP PWDs constitutes one spatial unit cell with a modulation traveling velocity of  $v_m = \omega_m/\kappa_m = 4.88$  m/s. As can be seen in Fig. 2(a), the displacement field captured at  $t = 0.005$  s with  $\delta = 1.5$  exhibits three distinct transmission channels, the frequency content of which is revealed using a fast Fourier transform (FFT). Hereafter, we omit  $q$  from the notation when  $q = 0$  since the fundamental harmonic matches the excitation frequency, i.e.,  $\omega^{(0)} = \omega$ . The normalized spectrum of the wave passing over the sensor locations indicated by the three green markers shows the fundamental harmonic ( $\omega/2\pi = 3$  kHz), first up-converted harmonic ( $\omega^{(+1)}/2\pi = 3.05$  kHz), and first down-converted harmonic ( $\omega^{(-1)}/2\pi = 2.95$  kHz) propagating along the  $\theta_A$ ,  $\theta_{A,+1}$  and  $\theta_{A,-1}$  directions, respectively. It is worth noting that sensors are placed at the the principal transmission angles given by  $\theta_{A,q}$  in the array's far field, i.e.,  $r \geq 1$  m. The FFT amplitudes of all three sensors

(obtained via FE simulations) are in near-perfect agreement with their counterparts computed using Eq. (4) as shown in Fig. 2(a). A visualization of the same is provided in Fig. 2(c), where the spatial distribution of FFT amplitudes are presented for different harmonics, confirming the predicted principal transmission directions (superposed as dashed black lines). For a modulation depth of  $\delta = 2.4$ , the fundamental harmonic completely disappears as a result of its vanishing directivity [ $J_0(2.4) \cong 0$ ]. This can also be confirmed by inspecting the corresponding FFT amplitudes in Figs. 2(b) and 2(d). Waves traveling in the broadside direction with small amplitudes are in fact side lobes of up- and down-converted transmission channels. For the parameters chosen here, the principal transmission directions calculated for second- and higher-order harmonics are complex. (Specifically for  $\kappa_c = 0$ ,  $\kappa_m = 20.4808\pi$ ,  $\omega_m/2\pi = 0.05$  kHz, and  $\omega/2\pi = 3$  kHz, principal transmission directions for second-order harmonics are computed as  $\theta_{A,-2} = -\pi/2 + i0.807$  and  $\theta_{A,+2} = \pi/2 - i0.757$ .) The physical implication of complex angles is that these channels propagate only along the array and eventually evanesce. They do not transmit energy due to the directivity of the PWD phased array.

## B. Reception

In order to investigate the STP PWD phased array's performance characteristics in reception mode, we consider a plane Lamb wave incident upon the array from an arbitrary direction  $\tilde{\theta}$  with respect to the broadside [see Fig. 2(e)]. Consistent with the previous analysis, we assume a sufficiently low frequency  $\tilde{\omega}$  enabling us to account for the first symmetric and antisymmetric Lamb waves only, with  $\tilde{k}_S$  or  $\tilde{k}_A$  as wave numbers, respectively. This results in the voltage signal received by the  $n$ th PWD at the corresponding location of  $(x, y) = (0, y_n)$  of the form

$$\tilde{v}_n(t) = t_R[\tilde{B}_S e^{i(-\tilde{\omega}t - \tilde{k}_S y_n \sin \tilde{\theta})} + \tilde{B}_A e^{i(-\tilde{\omega}t - \tilde{k}_A y_n \sin \tilde{\theta})}] \quad (6)$$

where  $\tilde{B}_\alpha$  is the amplitude and  $\tilde{k}_\alpha$  is the incident wave number of symmetric ( $\alpha = S$ ) or antisymmetric ( $\alpha = A$ ) waves. The displacement-to-voltage transfer function  $t_R$  is presumed to be identical for all array elements. The signal is then fed through the STP phase shifters, and following another Jacobi-Anger expansion, simplifies to

$$\begin{aligned} \tilde{v}_n(t) = & t_R \sum_{q=-\infty}^{\infty} i^q J_q(\delta) e^{i(-\tilde{\omega}^{(q)} t + \kappa_c^{[q]} y_n)} [\tilde{B}_S e^{-i\tilde{k}_S \sin \tilde{\theta} y_n} \\ & + \tilde{B}_A e^{-i\tilde{k}_A \sin \tilde{\theta} y_n}]. \end{aligned} \quad (7)$$

Finally, the output signal from the entire array is obtained by summing up all of the individual output signals, i.e.,  $\tilde{v}(t) = \sum_{n=1}^N \tilde{v}_n(t)$ , which becomes (see Note S1

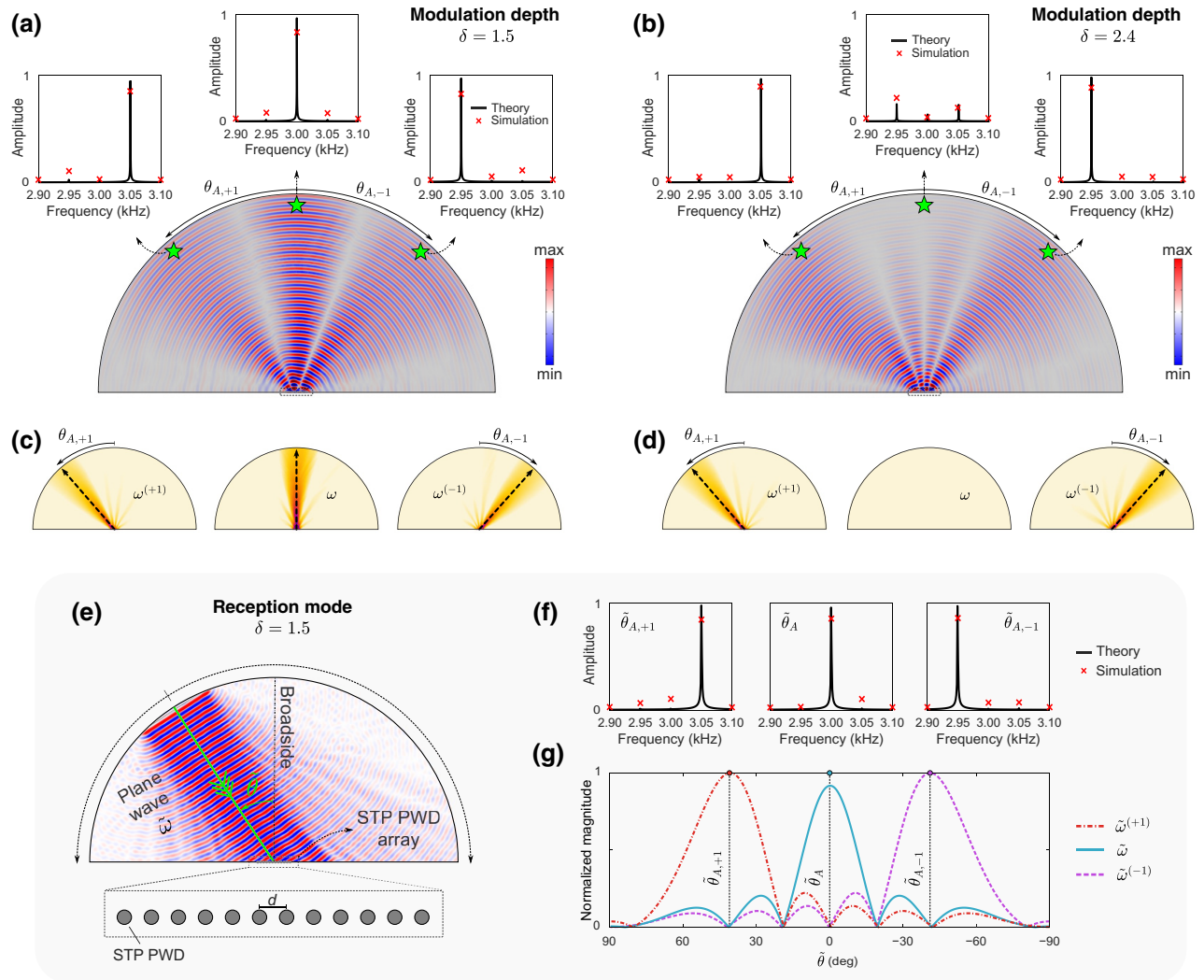


FIG. 2. STP PWD phased array in transmission and reception modes. (a),(b) Out-of-plane displacement field at  $t = 0.005$  s for a modulation depth of  $\delta = 1.5$  and  $\delta = 2.4$ , respectively. The insets show the normalized FFT amplitudes of sensor locations indicated by stars as predicted by both theory and simulations. (c),(d) Directional breakdown and distribution of the FFT amplitudes for up-converted, fundamental and down-converted harmonics when  $\delta = 1.5$  and  $\delta = 2.4$ , respectively. Theoretical principal transmission directions are plotted as dashed arrows for comparison. (e) Plane wave with a frequency of  $\tilde{\omega}$  incident upon the array from an arbitrary angle  $\tilde{\theta}$ . (f) From left to right: normalized FFT amplitudes (both theory and simulations) of received signal at output channel when the incoming plane wave is incident from  $\tilde{\theta}_{A,+1}$ ,  $\tilde{\theta}_A$  and  $\tilde{\theta}_{A,-1}$ , respectively. (g) FFT magnitude of received signal at the output channel as a function of the incident angle for different harmonics. Theoretical principal reception directions are plotted as dashed lines for comparison. Here,  $\omega/2\pi = \tilde{\omega}/2\pi = 3$  kHz,  $\omega^{(+1)}/2\pi = \tilde{\omega}^{(+1)}/2\pi = 3.05$  kHz,  $\omega^{(-1)}/2\pi = \tilde{\omega}^{(-1)}/2\pi = 2.95$  kHz.

within the Supplemental Material [62])

$$\tilde{v}(t) \cong t_R N \sum_{q=-\infty}^{\infty} [\tilde{B}_S \tilde{D}_{S,q}(\tilde{\theta}) + \tilde{B}_A \tilde{D}_{A,q}(\tilde{\theta})] e^{-i\tilde{\omega}^{(q)} t}, \quad (8)$$

where  $\tilde{D}_{\alpha,q}(\tilde{\theta})$  is the  $q$ th-order modified reception directivities of the STP PWD phased array for the first symmetric ( $\alpha = S$ ) and antisymmetric ( $\alpha = A$ ) Lamb waves; found

to be

$$\tilde{D}_{\alpha,q}(\tilde{\theta}) = i^q \mathbb{J}_q(\delta) \frac{\sin \left[ (Nd/2)(\tilde{k}_\alpha \sin \tilde{\theta} - \kappa_c^{[q]}) \right]}{N \sin \left[ (d/2)(\tilde{k}_\alpha \sin \tilde{\theta} - \kappa_c^{[q]}) \right]}, \quad \alpha = S, A. \quad (9)$$

Equation (9) resembles Eq. (5) albeit with wave numbers ( $\tilde{k}_\alpha$ ) that are not frequency shifted. Akin to the concept of principal transmission directions, we can define the principal reception directions as the angles along which

the STP PWD phased array is most sensitive to receiving incident waves. As such, we find the  $q$ th-order principal reception directions as  $\tilde{\theta}_{\alpha,q} = \sin^{-1}(\kappa_c^{[q]}/\tilde{k}_\alpha)$  with  $\alpha = S, A$  for symmetric and antisymmetric Lamb waves. The bottom panel of Fig. 2 depicts the behavior of the array operating in reception predicted from both theory and simulations. For evaluation purposes, the array is subjected to an antisymmetric wave incident at an arbitrary angle  $\tilde{\theta}$  and comprising a frequency of  $\tilde{\omega}/2\pi = 3$  kHz, as shown in Fig. 2(e). The previous 12 PWDs are utilized as receiving sensors. For each incident angle  $\tilde{\theta}$ , the received signals from PWDs are fed through their respective STP phase shifters and summed up at the output port. The FFT magnitudes of the array's output is provided in Fig. 2(g) as a function of  $\tilde{\theta}$  for three specific harmonics: the fundamental ( $\tilde{\omega}/2\pi = 3$  kHz), up-converted ( $\tilde{\omega}^{(+1)}/2\pi = 3.05$  kHz), and down-converted ( $\tilde{\omega}^{(-1)}/2\pi = 2.95$  kHz) channels. Owing to the linearity of the system dynamics, it immediately follows that FFT calculations can only be done at up- and down-conversions since other frequencies cannot be generated. The theoretical principal reception directions for first antisymmetric Lamb wave ( $\tilde{\theta}_A = 0^\circ$ ,  $\tilde{\theta}_{A,+1} = 41.4^\circ$ , and  $\tilde{\theta}_{A,-1} = -41.4^\circ$ ) are indicated on the figure as vertical dashed lines. We conclude that  $\tilde{\omega}^{(q)}$  is most effectively detected with a  $\tilde{\theta}_{A,q}$  incidence, where  $q \in \mathbb{Z}$ . To further elucidate this concept, Fig. 2(f) provides a comparison between the normalized FFT amplitudes of the received signal at the output channel as determined both theoretically and via FE simulations. (Here, the incoming wave is incident from the exact principal reception angles for the antisymmetric wave  $\tilde{\theta}_{A,q}$ .) In addition to the good agreement, we note that higher frequencies do not make a dominant appearance in the output spectrum; a phenomenon that is primarily attributed to the fact that higher harmonics do not have a real principal reception angle. For instance, the principal reception angle for the 3.10 kHz is calculated to be  $\pi/2 - i0.770$ , and for 2.90 kHz to be  $-\pi/2 + i0.770$ . The same can be confirmed by examining principal reception angles corresponding to higher harmonics. The nontrivial frequency conversion process taking place in an STP PWD phased array (during reception) is significant, particularly from a practical standpoint. Conventional phased arrays quasistatically sweep the value of  $\kappa_c$  to listen for omnidirectional incident waves. The proposed phased array with fixed parameters is potentially capable of the same by exploiting its reception features, specifically by analyzing only amplitudes of the various harmonics in the collected signal. If the parameters are tuned to the exact incident angles of multiple waves with the same frequency  $\tilde{\omega}$ , it becomes possible to clearly identify the dominant frequency relating to each incident direction as shown in Fig. 2(f); effectively surpassing the single-channel constraint typically exhibited by conventional arrays.

### III. EXPERIMENTAL ARRAY PERFORMANCE

The theoretical framework established earlier is validated through an experimental performance evaluation of the proposed STP PWD phased array. The array is constructed out of 12 PWDs (Manufacturer: Steminc Inc., Model: SMD05T04R111WL) forming two spatial unit cells, which are epoxy bonded (Manufacturer: 3M, Model: Scotch-Weld DP 270) to the center of an  $1066 \times 1066 \times 1.27$  mm<sup>3</sup> aluminum plate (5052 Aluminum Alloy). The complete setup is shown in Fig. 3 (see Note S5 within the Supplemental Material for details [62]). Note that the piezoelectric discs used in this work are capable of inducing in-plane radial strain, which can generate the required antisymmetric Lamb waves accordingly. Additionally, to minimize the amplitude of reflections, boundaries are covered with the damping material (Blu-Tack adhesive) to form a perfectly matched layer. In transmission, the elements of the array are excited using individual phase-modulated amplified harmonic signals with a frequency of  $\omega/2\pi = 3$  kHz. The excitations are generated by a custom driver controlled with a MATLAB code, which utilizes the Data Acquisition Toolbox. The phase-modulated signals are created digitally and then converted to analog signals using a D2A converter. The analog signals are amplified and tuned to generate a peak-to-peak voltage of  $V_{pp} \cong 14V$  for each channel. In order to visualize the elastic wave propagation, the out-of-plane velocity wave field is captured using a Polytec PSV-500 scanning laser Doppler vibrometer (SLDV), which is triggered from MATLAB's command line to ensure synchronized measurements with respect to the excitation signal. The measurements are taken over a scanning area of  $1000 \times 500$  mm<sup>2</sup> with a resolution of 12 points per wavelength (12 pt/ $\lambda$ ) and a sampling frequency of 100 kHz. The top panel of Fig. 4 presents the experimentally measured out-of-plane velocity wave field at  $t = 0.001$  s generated by the phased array in transmission corresponding to a modulation depth of  $\delta = 1.5$  (left) and  $\delta = 2.4$  (right). The closeup insets in both figures show the recorded measurements in both frequency and time domain for the three sensor locations depicted by the red, blue, and green discrete markers for the up-converted, fundamental and down-converted harmonics, respectively. The experimentally recorded wave fields as well as the frequency content of the generated harmonics show good agreement with predictions, i.e., both theoretical and simulation results presented in Fig. 2 for both modulation depths; thus validating the behavior of the array in transmission mode (see Movies S1 and S2 within the Supplemental Material for the transient response in transmission mode [62]). In reception, incident plane waves with an excitation frequency of  $\tilde{\omega}/2\pi = 3$  kHz are generated using two arrays of piezoelectric discs, which are bonded to the plate at angles of  $41^\circ$  and  $-41^\circ$  (principal reception directions), respectively, with respect to the

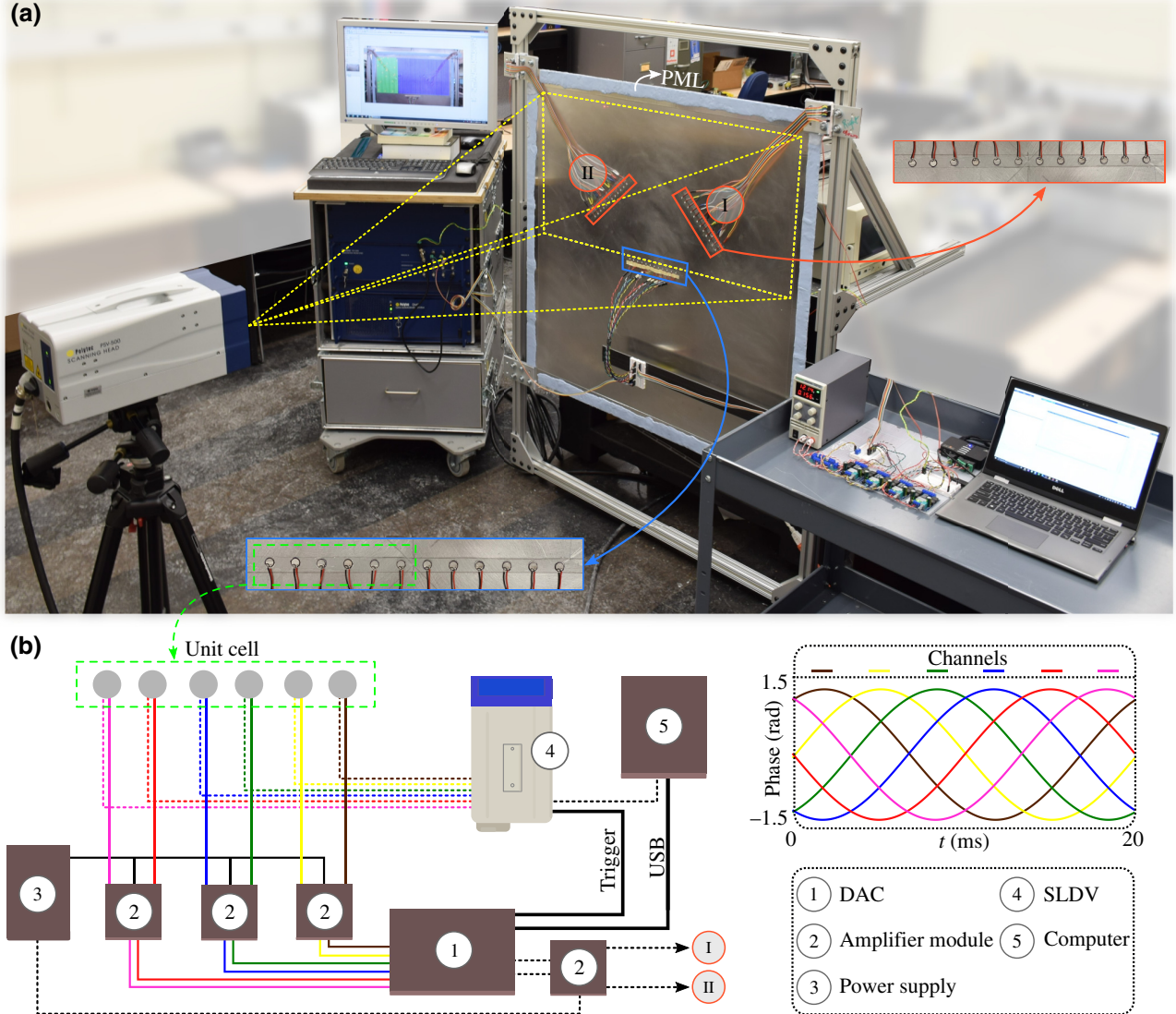


FIG. 3. Experimental setup. (a) Illustration of the experimental setup showing the aluminum plate under study, mounting setup, laser vibrometer system (SLDV), controller circuit, and the perfectly matched layer (PML). The STP PWD phased array is highlighted in the closeup using blue lines. The arrays used for generating incident waves in reception are highlighted in dashed red boxes. (b) Schematic diagram of the controller circuit. Solid lines represent the circuit for the transmission experiment, dashed lines represent the circuit for the reception experiment, and the thicker lines represent the connections that remain constant for both experiments. (I) and (II) refer to the arrays generating the different incident waves shown in (a) for the reception experiment. The individual piezoelectric connections in the schematic diagram and their respective phase signals are color coded for clarity.

broadside. Once the incident wave reaches the STP PWD phased array, the signals are recorded and postprocessed to augment the STP phase modulation and then summed up to yield the net voltage signal. The bottom panel of Fig. 4 shows incoming wave fields incident upon the STP PWD array from the principal reception directions:  $\tilde{\theta}_{A,+1}$  (left) and  $\tilde{\theta}_{A,-1}$  (right). In these figures, insets in the top left corner depict the postprocessed modulated signals collected from each channel of the STP PWD phased array in light pink (background lines) and the collected voltage  $\tilde{v}(t)$  in magenta (foreground line). The collected voltage

signal from the output port is the total sum of the individual modulated signals, which can be analyzed to estimate the direction of arrival. The top-right insets show the collected voltage (unmodulated) from the first (navy-blue) and last (maroon) elements of the phased array. An inherent phase shift can be observed due to the direction of incidence of the incoming wave. For example, when the direction of incidence is  $\tilde{\theta}_{A,+1}$  ( $\tilde{\theta}_{A,-1}$ ), the waves first reach the first (last) piezodisc before reaching the last (first) one, which explains the phase shift in the recorded signals. The bottom insets show the normalized FFT amplitude of the collected

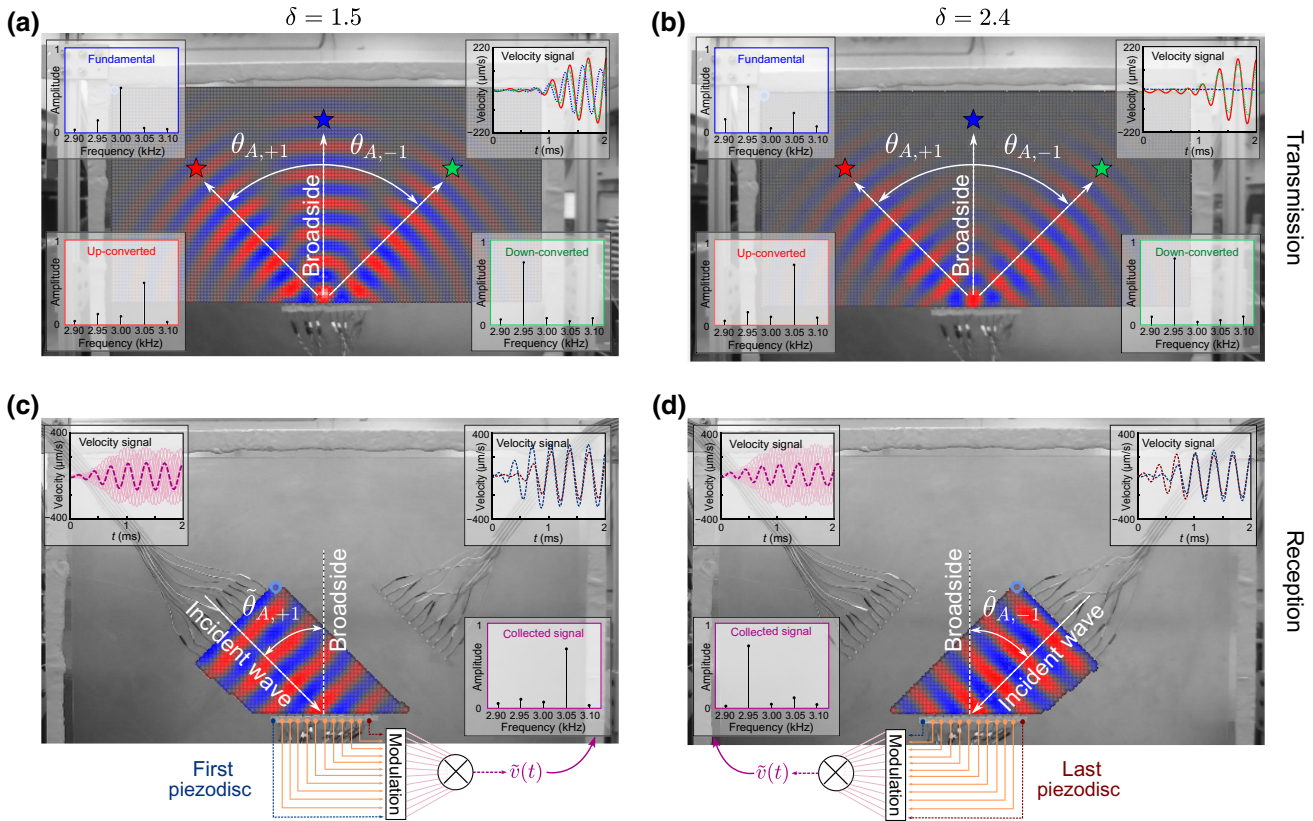


FIG. 4. Experimental performance of the dynamic array. (a),(b) Out-of-plane velocity wave field for  $\delta = 1.5$  and  $\delta = 2.4$  at  $t = 0.001$  s. In (a) and (b), the insets show time- and frequency-domain measurements at sensor locations indicated by the red, blue, and green markers, which are placed at a radial distance of 450 mm from the center of the plate at principal transmission directions. (c),(d) Out-of-plane velocity wave fields of the generated incident waves approaching the array from principal reception directions. In (c) and (d), the top-left insets show the postprocessed individually modulated signals for each of the channels in light pink and the collected voltage signal in magenta. The top-right insets show the unmodulated signal from the first (navy-blue) and last (maroon) elements of the phased array. The bottom insets show the normalized FFT amplitude of the collected voltage signal at the output port. All parameters are the same as those used in Fig. 2.

signal at the output port, indicating a frequency conversion, and is utilized to estimate the direction of arrival of the incident wave. These results validate the theoretical findings presented in Fig. 2 for the behavior of the array in reception mode (see Movies S3 and S4 within the Supplemental Material for the transient response during reception).

#### IV. WAVE BEAMING AND MULTICHANNEL NONRECIPROCITY

To demonstrate the capabilities of the STP PWD array to instigate some form of wave nonreciprocity, we examine its response in transmission mode to its counterpart when operating under a time-reversed signal. Figure 5(a) shows the transmission channels of the array operating at  $\delta = 1.5$  as a result of an input voltage carrying a fundamental frequency  $\omega$ . As anticipated, three distinct waves with different frequencies are observed, each propagating in its respective principal transmission direction,  $\theta_{A,q}$ . We

then examine the array's output when a time-reversed version of either of these transmitted waves are incident upon the array [i.e., incident plane waves with the same frequency traveling in reverse direction towards the array, as shown in Fig. 5(b)]. The angle of incidence associated with the fundamental wave  $\omega$  is  $\theta_A$ , which is received with the same frequency as shown in the middle panel of Fig. 5(b); reasserting the reciprocal behavior within the array's fundamental channel. A comparison between the frequency content of the output voltage signal in reception of each of the cases with the input signal in transmission ( $\omega$ ) reveals the nonreciprocal nature of the proposed array. On the other hand, the angle of incidence associated with the up-converted wave is  $\theta_{A,+1}$ , which is received with a predominant frequency of  $\omega^{(+2)}$  [leftmost panel of Fig. 5(b)]. This double up-conversion is a direct manifestation of the induced bias in the system. A similar pattern can be observed for the down-converted wave, which at reception shows a spectrum dominated by  $\omega^{(-2)}$  [rightmost panel of Fig. 5(b)]. The same conclusions pertaining to the

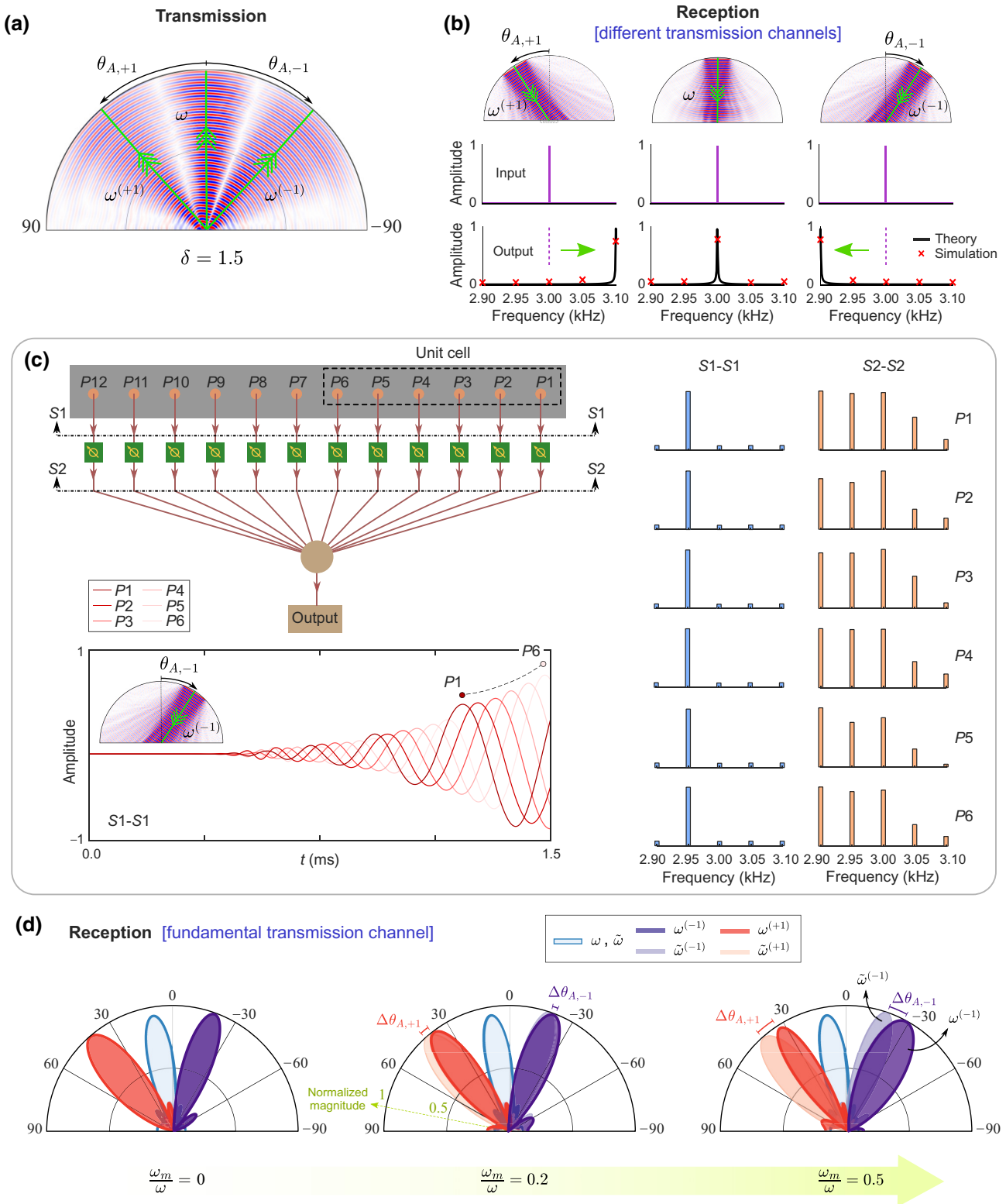


FIG. 5. Nonreciprocal wave beaming in the STP PWD phased array. (a) Transmission channels as a result of an input voltage signal with frequency of  $\omega$ . (b) Reception process and normalized FFT amplitudes (as predicted from both theory and simulations) of received signal at the output port corresponding to different transmission channels. (c) Characteristics of the received signal in different stages of the reception process. (d) Effect of temporal modulation speed on the radiation and reception patterns of the STP PWD phased array. The parameter used are as follows:  $\omega/2\pi = \tilde{\omega}/2\pi = 3$  kHz,  $\omega^{(+1)}/2\pi = \tilde{\omega}^{(+1)}/2\pi = 3.05$  kHz,  $\omega^{(-1)}/2\pi = \tilde{\omega}^{(-1)}/2\pi = 2.95$  kHz,  $\kappa_c = 5.4113\pi$ ,  $\kappa_m = 15.4821\pi$ , and  $\delta = 1.5$ .

array's behavior in reception mode can be arrived at using Eq. (8), as detailed in Note S4 within the Supplemental Material [62]. Figure 5(c) illustrates the characteristics of the signal at different stages of the reception process in both frequency (right panel) and time (left panel) domains. The received signal is fed through the STP phase shifters and finally collected at the output port.

Another way to quantify the reciprocity of the system (or lack thereof) is via the extent to which radiation and reception patterns are identical within a given array. The STP PWD array is capable of breaking reciprocity by introducing different principal transmission and reception directions. We examine the antisymmetric Lamb waves and define  $\Delta\theta_{A,q}$  as the difference between the principal transmission and reception angles, i.e.,  $\Delta\theta_{A,q} = \theta_{A,q} - \tilde{\theta}_{A,q}$ . For the special case corresponding to  $\tilde{\omega} = \omega$ ,  $\Delta\theta_{A,q}$  is nonzero for all values of  $q \neq 0$  and is proportional to the ratio of  $\omega_m/\omega$ . As anticipated,  $\Delta\theta_{A,q}$  vanishes at  $q = 0$ , which is reminiscent of the behavior of conventional phased arrays. To further illustrate, Fig. 5(d) demonstrates the effect of the modulation frequency ratio  $\omega_m/\omega$  on both radiation and reception patterns of an STP PWD phased array, which perfectly coincide at  $\omega_m/\omega = 0$  (demonstrating a fully reciprocal response). As the modulation frequency ratio increases, the difference between the principal angles becomes more stark since  $\Delta\theta_{A,q}$  takes on nonzero values for up- and down-converted waves. In effect, the dissimilarity between radiation and reception patterns, and consequently the degree of nonreciprocity, becomes stronger with faster modulation.

## V. CONCLUSION

In summary, a conventional PWD phased array transmits guided waves in a desired direction by augmenting the individual voltage signals inputted to each array element by a static phase gradient  $\kappa_c$ . For the same set of parameters, it can *only* listen for guided waves arriving from the same exact direction. In contrast, in an STP PWD phased array, the individual input voltage signals for the PWDs are augmented with a dynamically varying phase angle, enabling an intentional breakage of elastooptic reciprocity and establishing independent (and tunable) radiation and reception patterns, while simultaneously allowing for multiple-channel operation in both transmission and reception regimes.

## ACKNOWLEDGMENTS

The authors acknowledge support of this work from the US National Science Foundation through Awards No. 1847254 (CAREER) and No. 1904254, as well as support from the University at Buffalo (SUNY) through the Buffalo Blue Sky Program.

M.M., R.A., and M.A.A. carried out the analysis and performed the calculations. M.M. and R.A. planned the experiments, constructed the setup, and conducted the measurements. All authors contributed to interpretation of the results. A.A. and M.N. supervised the project. The paper was written with input from all authors.

- 
- [1] V. Giurgiutiu, *Structural Health Monitoring: With Piezoelectric Wafer Active Sensors* (Academic Press, Cambridge, MA, USA, 2007).
  - [2] J. He, D. C. Rocha, and P. Sava, Guided wave tomography based on least-squares reverse-time migration, *Struct. Health Monit.* **19**, 1237 (2020).
  - [3] Q. Chen, K. Xu, and D. Ta, High-resolution lamb waves dispersion curves estimation and elastic property inversion, *Ultrasonics* **115**, 106427 (2021).
  - [4] M. Mazzotti, C. Sugino, E. Kohtanen, A. Erturk, and M. Ruzzene, Experimental identification of high order lamb waves and estimation of the mechanical properties of a dry human skull, *Ultrasonics* **113**, 106343 (2021).
  - [5] C. He, X. Zhang, Y. Lu, B. Wu, and Y.-C. Lee, Sound fields radiated from a linear phased array based on analytical solutions of transient elastic waves, *Wave Motion* **73**, 86 (2017).
  - [6] Z. Tian and L. Yu, Elastic Phased Diffraction Gratings for Manipulation of Ultrasonic Guided Waves in Solids, *Phys. Rev. Appl.* **11**, 024052 (2019).
  - [7] X. Cao, C. Jia, H. Miao, G. Kang, and C. Zhang, Excitation and manipulation of guided shear-horizontal plane wave using elastic metasurfaces, *Smart Mater. Struct.* **30**, 055013 (2021).
  - [8] X. Qing, W. Li, Y. Wang, and H. Sun, Piezoelectric transducer-based structural health monitoring for aircraft applications, *Sensors* **19**, 545 (2019).
  - [9] T. Sun, F. Tasnim, R. T. McIntosh, N. Amiri, D. Solav, M. T. Anbarani, D. Sadat, L. Zhang, Y. Gu, and M. A. Karamiet *et al.*, Decoding of facial strains via conformable piezoelectric interfaces, *Nat. Biomed. Eng.* **4**, 954 (2020).
  - [10] T. Omirou, A. Marzo, S. A. Seah, and S. Subramanian, in *Proceedings of the 33rd Annual ACM Conference on Human Factors in Computing Systems* (Association for Computing Machinery, New York, NY, United States, Seoul, 2015), p. 309.
  - [11] A. Marzo, S. A. Seah, B. W. Drinkwater, D. R. Sahoo, B. Long, and S. Subramanian, Holographic acoustic elements for manipulation of levitated objects, *Nat. Commun.* **6**, 1 (2015).
  - [12] K. F. Braun, Electrical oscillations and wireless telegraphy, *Nobel Lect.*, December **11**, 226 (1909).
  - [13] R. Mailloux, *Phased Array Antenna Handbook*, Artech House Antennas and Electromagnetics Analysis Library (Artech House Publishers, Norwood, MA, USA, 2017), 3rd ed.
  - [14] S.-C. Wooh and Y. Shi, Optimum beam steering of linear phased arrays, *Wave Motion* **29**, 245 (1999).
  - [15] C. V. Poulton, A. Yaacobi, D. B. Cole, M. J. Byrd, M. Raval, D. Vermeulen, and M. R. Watts, Coherent solid-state

- lidar with silicon photonic optical phased arrays, *Opt. Lett.* **42**, 4091 (2017).
- [16] A. Hassanien and S. A. Vorobyov, Phased-mimo radar: A tradeoff between phased-array and mimo radars, *IEEE Trans. Signal Process.* **58**, 3137 (2010).
- [17] T. M. Rynne, J. F. Spadaro, J. L. Iovenitti, J. P. Dering, and D. G. Hill, Phased array approach to retrieve gases, liquids, or solids from subaqueous geologic or man-made formations, US Patent 5,826,653 (1998).
- [18] L. Yu and V. Giurgiutiu, In situ 2-d piezoelectric wafer active sensors arrays for guided wave damage detection, *Ultrasonics* **48**, 117 (2008).
- [19] L. Yu and V. Giurgiutiu, In-situ optimized pwas phased arrays for lamb wave structural health monitoring, *J. Mech. Mater. Struct.* **2**, 459 (2007).
- [20] A. Purekar, D. Pines, S. Sundararaman, and D. Adams, Directional piezoelectric phased array filters for detecting damage in isotropic plates, *Smart Mater. Struct.* **13**, 838 (2004).
- [21] Q. Huan, M. Chen, Z. Su, and F. Li, A high-resolution structural health monitoring system based on sh wave piezoelectric transducers phased array, *Ultrasonics* **97**, 29 (2019).
- [22] X. Zhang, W. Zhou, H. Li, and Y. Zhang, Guided wave-based bend detection in pipes using in-plane shear piezoelectric wafers, *NDT E Int.* **116**, 102312 (2020).
- [23] M. Vahedi, R. Ardestani, and S. M. Zahrai, Sensitivity analysis of tubular-web reduced beam section connections under cyclic loading, *Int. J. Steel Struct.* **1**, 100 (2020).
- [24] J. Hu, H. Peng, X. Yao, T. Liu, P. Lu, and C. Zhao, An investigation to the design of high-precision wind sensing device based on piezoelectric array, *Trans. Inst. Meas. Control* **42**, 840 (2020).
- [25] Y. Ohara, M. C. Remillieux, T. Onuma, K. Tsunoda, T. Tsuji, and T. Mihara, Toward an ultra-high resolution phased-array system for 3d ultrasonic imaging of solids, *Appl. Phys. Lett.* **117**, 111902 (2020).
- [26] Y. Ohara, S. Yamamoto, T. Mihara, and K. Yamanaka, Ultrasonic evaluation of closed cracks using subharmonic phased array, *Jpn. J. Appl. Phys.* **47**, 3908 (2008).
- [27] O. Buck, W. Morris, and J. M. Richardson, Acoustic harmonic generation at unbonded interfaces and fatigue cracks, *Appl. Phys. Lett.* **33**, 371 (1978).
- [28] S. Biwa, S. Nakajima, and N. Ohno, On the acoustic nonlinearity of solid-solid contact with pressure-dependent interface stiffness, *J. Appl. Mech.* **71**, 508 (2004).
- [29] H. Kazari, M. Kabir, A. Mostavi, and D. Ozevin, Multi-frequency piezoelectric micromachined ultrasonic transducers, *IEEE Sens. J.* **19**, 11090 (2019).
- [30] Y. Ohara, H. Nakajima, T. Tsuji, and T. Mihara, Nonlinear surface-acoustic-wave phased array with fixed-voltage fundamental wave amplitude difference for imaging closed cracks, *NDT E Int.* **108**, 102170 (2019).
- [31] J. Cheng, J. N. Potter, A. J. Croxford, and B. W. Drinkwater, Monitoring fatigue crack growth using nonlinear ultrasonic phased array imaging, *Smart Mater. Struct.* **26**, 055006 (2017).
- [32] S. Haupert, G. Renaud, and A. Schumm, Ultrasonic imaging of nonlinear scatterers buried in a medium, *NDT E Int.* **87**, 1 (2017).
- [33] Y. Ohara, H. Nakajima, S. Haupert, T. Tsuji, and T. Mihara, Imaging of three-dimensional crack open/closed distribution by nonlinear ultrasonic phased array based on fundamental wave amplitude difference, *Jpn. J. Appl. Phys.* **59**, SKKB01 (2020).
- [34] C. Bruno, A. Gliozzi, M. Scalerandi, and P. Antonaci, Analysis of elastic nonlinearity using the scaling subtraction method, *Phys. Rev. B* **79**, 064108 (2009).
- [35] J. Achenbach and J. Achenbach, *Reciprocity in Elastodynamics* (Cambridge University Press, Cambridge, UK, 2003).
- [36] J. D. Adam, L. E. Davis, G. F. Dionne, E. F. Schloemann, and S. N. Stitzer, Ferrite devices and materials, *IEEE Trans. Microw. Theory Tech.* **50**, 721 (2002).
- [37] D. L. Sounas and A. Alù, Non-reciprocal photonics based on time modulation, *Nat. Photonics* **11**, 774 (2017).
- [38] N. Antonellis, R. Thomas, M. Kats, I. Vitebskiy, and T. Kottos, Nonreciprocity in Photonic Structures with Phase-Change Components, *Phys. Rev. Appl.* **11**, 024046 (2019).
- [39] C. Sanavio, V. Peano, and A. Xuereb, Nonreciprocal topological phononics in optomechanical arrays, *Phys. Rev. B* **101**, 085108 (2020).
- [40] X. Zhu, J. Li, C. Shen, X. Peng, A. Song, L. Li, and S. A. Cummer, Non-reciprocal acoustic transmission via space-time modulated membranes, *Appl. Phys. Lett.* **116**, 034101 (2020).
- [41] L. Shao, W. Mao, S. Maity, N. Sinclair, Y. Hu, L. Yang, and M. Loncar, in *CLEO: QELS\_Fundamental Science* (Optical Society of America, Washington, DC, 2020), p. FTh4Q-2.
- [42] R. Fleury, D. L. Sounas, C. F. Sieck, M. R. Haberman, and A. Alù, Sound isolation and giant linear nonreciprocity in a compact acoustic circulator, *Science* **343**, 516 (2014).
- [43] Z. Yang, F. Gao, X. Shi, X. Lin, Z. Gao, Y. Chong, and B. Zhang, Topological Acoustics, *Phys. Rev. Lett.* **114**, 114301 (2015).
- [44] R. Fleury, D. Sounas, M. R. Haberman, and A. Alù, Nonreciprocal acoustics, *Acoust. Today* **11**, 14 (2015).
- [45] A. Sasmal, N. Geib, B.-I. Popa, and K. Grosh, Broadband nonreciprocal linear acoustics through a non-local active metamaterial, *New J. Phys.* **22**, 063010 (2020).
- [46] M. Attarzadeh, S. Maleki, J. Crassidis, and M. Nouh, Non-reciprocal wave phenomena in energy self-reliant gyric metamaterials, *J. Acoust. Soc. Am.* **146**, 789 (2019).
- [47] H. Nassar, B. Yousefzadeh, R. Fleury, M. Ruzzene, A. Alù, C. Daraio, A. N. Norris, G. Huang, and M. R. Haberman, Nonreciprocity in acoustic and elastic materials, *Nat. Rev. Mater.* **5**, 667 (2020).
- [48] Y. Chen, X. Li, G. Hu, M. R. Haberman, and G. Huang, An active mechanical willis meta-layer with asymmetric polarizabilities, *Nat. Commun.* **11**, 1 (2020).
- [49] A. Palermo, P. Celli, B. Yousefzadeh, C. Daraio, and A. Marzani, Surface wave non-reciprocity via time-modulated metamaterials, *J. Mech. Phys. Solids* **145**, 104181 (2020).
- [50] M. Attarzadeh, J. Callanan, and M. Nouh, Experimental Observation of Nonreciprocal Waves in a Resonant Metamaterial Beam, *Phys. Rev. Appl.* **13**, 021001 (2020).

- [51] D.-W. Wang, H.-T. Zhou, M.-J. Guo, J.-X. Zhang, J. Evers, and S.-Y. Zhu, Optical Diode Made from a Moving Photonic Crystal, *Phys. Rev. Lett.* **110**, 093901 (2013).
- [52] E. Riva, M. Di Ronco, A. Elabd, G. Cazzulani, and F. Braghin, Non-reciprocal wave propagation in discretely modulated spatiotemporal plates, *J. Sound Vib.* **471**, 115186 (2020).
- [53] A. M. Shaltout, V. M. Shalaev, and M. L. Brongersma, Spatiotemporal light control with active metasurfaces, *Science* **364**, 1 (2019).
- [54] X. Wang, A. Díaz-Rubio, H. Li, S. A. Tretyakov, and A. Alù, Theory and Design of Multifunctional Space-Time Metasurfaces, *Phys. Rev. Appl.* **13**, 044040 (2020).
- [55] A. E. Cardin, S. R. Silva, S. R. Vardeny, W. J. Padilla, A. Saxena, A. J. Taylor, W. J. Kort-Kamp, H.-T. Chen, D. A. Dalvit, and A. K. Azad, Surface-wave-assisted nonreciprocity in spatio-temporally modulated metasurfaces, *Nat. Commun.* **11**, 1 (2020).
- [56] V. Tiukuvaara, T. J. Smy, and S. Gupta, Floquet analysis of space-time modulated huygens' metasurfaces with lorentz dispersion, ArXiv:2007.07063 (2020).
- [57] J. Zang, A. Alvarez-Melcon, and J. Gomez-Diaz, Nonreciprocal Phased-Array Antennas, *Phys. Rev. Appl.* **12**, 054008 (2019).
- [58] C. A. Balanis, *Antenna Theory: Analysis and Design* (John Wiley & Sons, Hoboken, NJ, USA, 2016).
- [59] R. Adlakha, M. Moghaddaszadeh, M. A. Attarzadeh, A. Aref, and M. Nouh, Frequency selective wave beaming in nonreciprocal acoustic phased arrays, *Sci. Rep.* **10**, 1 (2020).
- [60] R. Adlakha, M. Moghaddaszadeh, M. Attarzadeh, A. Aref, and M. Nouh, in *ASME International Mechanical Engineering Congress and Exposition* (American Society of Mechanical Engineers, Portland, OR, 2020), Vol. 84478, p. V001T01A016.
- [61] C. Rasmussen, L. Quan, and A. Alù, Acoustic nonreciprocity, *J. Appl. Phys.* **129**, 210903 (2021).
- [62] See Supplemental Material at <http://link.aps.org/supplemental/10.1103/PhysRevApplied.16.034033> for extended methods and videos.
- [63] J. L. Rose, *Ultrasonic Guided Waves in Solid Media* (Cambridge University Press, Cambridge, UK, 2014).